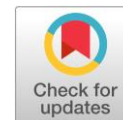


Kinetics of solid-state oxidation of iron, copper and zinc sulfide mixture

Alexander M. Klyushnikov , Sergey M. Pikalov , Roza I. Gulyaeva * 

Laboratory of Non-Ferrous Metals Pyrometallurgy, Department of Non-Ferrous Metals, Institute of Metallurgy of the Ural Branch of the Russian Academy of Sciences, Ekaterinburg 620016, Russia

* Corresponding author: amk8@mail.ru



This paper belongs to a Regular Issue.

Abstract

The kinetics of solid-state oxidation by air of iron, copper and zinc sulfide natural mixture, which is typical of the pyritic copper ores, is investigated. Using the high-temperature X-ray powder diffraction, thermogravimetry and differential scanning calorimetry, it was found that the process can be represented by five exothermic elementary reactions, corresponding to intensive burning of iron, copper and zinc sulfides, and two endothermic ones, associated with decomposition of copper and iron sulfates. Kinetic analysis is performed by Kissinger and Augis–Bennett methods, the model-free function mechanism was determined from $y(\alpha)$ master plots and iterative optimization of the kinetic parameters. The limiting steps of these reactions are nucleation and crystal growth, and the values of activation energy, pre-exponential factor and Avrami exponent are in the ranges of 140–459 kJ·mol⁻¹, 1.41·10⁴–3.49·10³¹ s⁻¹, and 1.0–1.7, respectively. Crystallization is followed by an increase in the number of nuclei, which may be formed both at the interface and in the bulk of the ore particles, and crystal growth is one-dimensional and controlled by a chemical reaction at the phase boundary or diffusion. The results of the work can contribute to the development of theoretical ideas about the physicochemical transformations of pyritic ores and concentrates during pyrometallurgical operations.

Keywords

iron sulfide
copper sulfide
zinc sulfide
pyritic copper ore
oxidation
kinetics

Key findings

- The formal kinetics of the sulfides, oxidation is attributed to seven elementary reactions.
- The activation energy of the elementary reactions is 140–459 kJ·mol⁻¹.
- The limiting steps of the elementary reactions are nucleation and crystal growth.
- Nuclei may be formed both at the interface and in the volume of the ore particles.
- Crystal growth is one-dimensional and is controlled by a chemical reaction or diffusion.

© 2023, the Authors. This article is published in open access under the terms and conditions of the Creative Commons Attribution (CC BY) license (<http://creativecommons.org/licenses/by/4.0/>).

1. Introduction

Currently, pyritic copper ores are primarily processed according to the scheme that includes the following operations: comminuting and froth flotation of initial ore with the separation of sulfide concentrate, autogenous matte smelting of the concentrate, converting of the matte into blister copper, and fire refining and electrorefining of the blister copper to cathode copper. The matte smelting and converting slags are depleted by flotation, the resulting concentrates are returned to matte smelting, and the

depleted slag is sent to the dump. The off-gases from matte smelting and converting are utilized in the production of sulfuric acid. The final products of the technology are cathode copper, slags, sulfuric acid, and electrolytic slime that concentrates precious and rare metals [1].

Massive and disseminated ores of pyritic copper deposits from the Urals region (Russia) may have an increased (up to 0.2 mass%) content of cobalt [2, 3], and there is a need for its associated extraction in commercial products. The cobalt output channel in the scheme described above is the converter slag; smelting with a carbonaceous reducing

agent and a sulfidizer (sulfide concentrate) can be used to extract a cobalt-rich sulfide product suitable for processing by conventional methods. The problem is that the fine intergrowth of ore minerals and high solubility of non-ferrous metals in pyrite are the reasons of transition of up to 95% of cobalt into the waste products during flotation of the ores [4]. Processing the entire mass of the ore according to the described scheme is limited for technological and economic reasons.

A promising route for the processing of pyritic copper ores from the Urals can be their direct partial oxidative roasting in a fluidized bed furnace at 800–900 °C with the transfer of up to 80% of sulfur into the gas phase (in this case, a significant part of the calorific capacity of the ore will be used) and the use of the resulting calcine as a sulfidizing agent in the reduction-sulfiding smelting of oxidized nickel-cobalt ores (laterites) from the deposits of the same region, which are not currently processed [5]. Varying the proportions of the roasted pyrite ore and oxidized nickel-cobalt ore in the feed of matte smelting will allow: i) regulating the yields and compositions of the smelting products; ii) controlling sulfur distribution, where most of the sulfur in the form of SO₂-rich roasting gases will be directed to manufacturing sulfuric acid, and the remainder will be spent for nickel and cobalt sulfiding of oxidized nickel ore during matte smelting; iii) extracting nickel, copper, cobalt and precious metals into the matte containing up to 10 mass% Ni+Cu+Co (at the same time, the presence of copper in the matte will reduce the loss of nickel and cobalt in slag [6]); iv) eliminating or minimizing the need for fluxes by using the fluxing potential of the ores; v) obtaining the final slag in the final step of the scheme [7, 8]. We have conducted research towards the development of the scientific basis and the feasibility study of this method [9–13]. An important aspect of the technology is the intensity of oxidative roasting of the copper ore, which determines the specific productivity of the fluidized bed furnace and temperature and duration of the process; for its evaluation, information on the chemistry, kinetics, and mechanism of roasting is needed. A lot of publications are devoted to these questions in relation to copper-nickel ores [14], copper [15–27], zinc [17, 28, 29], nickel [30, 31], and copper-cobalt [32] concentrates, as well as individual sulfide minerals which are part of them: pyrite [33–46], marcasite [47], mackinawite [48], pyrrhotite [34, 36, 39, 49–54], chalcopyrite [36, 47, 55–59], covellite [60], chalcocite [47, 60–62], zinc sulfide [63–69], cobalt sulfide [70], and their mixtures [71, 72]. The purpose of the present work is to study the kinetics and mechanism of solid-state oxidation of iron, copper and zinc sulfide natural mixture, typical of the pyritic copper ores.

2. Experimental

For the study, a representative sample of a pyritic copper ore from the Dergamysh deposit (Russia) was taken; the

sample was ground in a laboratory mill to a particle size of less than 0.1 mm.

The chemical composition of the ore sample was investigated by inductively coupled plasma atomic emission spectrometry (ICP AES) on an iCAP 6300 Duo optical emission spectrometer (Thermo Scientific). Preparations for analysis were carried out by dissolving a sample weighing 0.1 g in a mixture of mineral acids.

The thermal properties of the ore sample were studied by the method of simultaneous thermogravimetry (TG) and differential scanning calorimetry (DSC) on a STA 449 C Jupiter[®] instrument for synchronous thermal analysis (NETZSCH). For measurements, about 8.4 mg of the sample was distributed in a thin layer at the bottom of a corundum crucible, after which the crucible was placed into the measurement cell of the instrument and heated from 30 to 1100 °C at a rate of $\beta_i = 5, 10, \text{ and } 20 \text{ } ^\circ\text{C}\cdot\text{min}^{-1}$ (hereinafter, the subscript "i" denotes the i-th temperature program ($i = 1, 2, 3$)). Dynamic oxidizing atmosphere in the reaction space was maintained by blowing the measurement cell with dried synthetic air (21 vol% O₂, 79 vol% N₂) supplied at a flow rate of 30 cm³·min⁻¹. The empty reference crucible was the same as the sample crucible. The DSC correction parameters were estimated from the enthalpy of fusion of chemically pure (99.99 mass%) indium using the NETZSCH Thermokinetics 3.0 software. The composition of gases evolved during heating was evaluated by mass spectrometry (MS), for which a quadrupole QMS 403 C Aëolos[®] mass spectrometer (NETZSCH) was coupled with the thermal analyzer; ionic current (I , A) of gases (H₂O, CO₂, SO₂, and SO₃) released during heating and oxidation of the ore was measured in the mode of given mass numbers. The processing of the measurement results was made using the NETZSCH Proteus[®] 5.1 software, including the identification of the onset (T_o , °C), maximum (T_p , °C), and endset (T_e , °C) temperatures, and areas (ΔH , J·g⁻¹) for DSC peaks, relative mass changes (Δm , %), and peak temperatures ($T_p^{\text{H}_2\text{O}}$, $T_p^{\text{CO}_2}$, $T_p^{\text{SO}_2}$, and $T_p^{\text{SO}_3}$, °C) of the ionic current curves of H₂O, CO₂, SO₂, and SO₃. Separation of complex DSC peaks into their constituent overlapping elementary peaks and determination of their onset (T_{oij} , °C), maximum ($T_{p ij}$, °C), and endset ($T_{e ij}$, °C) temperatures, as well as the values of their full width at the half of maximum ($\Delta T_{p ij}$, °C) were performed using the MathWorks software according to the method outlined in [73]. The baseline was characterized by a linear function, and the profile of elementary peaks was approximated by Frazer–Suzuki (asymmetric Gaussian) function. For each temperature, the value of the function describing the complex peak was elaborated as the sum of such values for elementary peaks, and the reliability of approximation (for significance level $\alpha = 5\%$) was controlled by the value of Pearson correlation coefficient (r). The measurement error was ± 0.01 mg for mass, ± 3 °C for temperature, and $\pm 5\%$ for heat.

The phase composition of the ore sample was determined by X-ray powder diffraction (XRD) on DRON-2.0 X-

ray diffractometer. Experiments on oxidative roasting of the ore combined with evaluation of the phase composition of the products using high-temperature XRD (HTXRD) method were performed in the high-temperature UVD-2000 setup mounted on the above device, equipped with a resistance furnace with a platinum heating element; the design of the setup provided free atmospheric air access to the working chamber. The experiment included heating the initial ore at an average rate of $10\text{ }^{\circ}\text{C}\cdot\text{min}^{-1}$ from $25\text{ }^{\circ}\text{C}$ to a given temperature (100, 200, 300, 400, 500, 600, 700, 800, and $900\text{ }^{\circ}\text{C}$) and isothermal dwelling at this temperature for 80 min. At the same time, as mentioned above, *in situ* diffractograms were recorded in the isothermal sections of the cycles. The measurements were conducted in the following mode: Bragg–Brentano geometry; Cu $K\alpha$ radiation ($\lambda_{\alpha} = 1.54056\text{ \AA}$); graphite monochromator on the output beam; tube voltage and current of 30 kV and 30 mA, respectively; angular range (2θ) and step (2θ) of $10\text{--}90^{\circ}$ and 0.02° , and point exposure time of 2 s at $25\text{ }^{\circ}\text{C}$ and 1.2 s for high-temperature measurements. The samples for the experiment were prepared by applying 1–3 mg of a powdery ($<0.1\text{ mm}$ particle size) material to a substrate made of plexiglas or $(\text{Zr},\text{Y})\text{O}_{2-x}$. The temperature was measured with a type S thermocouple, the hot junction of which was placed near the sample (the measurement error was $\pm 2\text{ }^{\circ}\text{C}$). Phase identification and semi-quantitative (with an error of ± 5 relative %) estimation of the contents in the crystal component of the samples were performed by the reference intensity ratio (RIR) method [74, 75] using the QualX 2.0 software [76] and the Pow_Cod database [76]. Based on HTXRD data, a possible sequence of chemical reactions taking place at the studied temperatures was established; the values of reaction equilibrium constants (K_T) at temperature T (K) were calculated using the HSC Chemistry 6.12 package (Outotec Research Oy).

The microstructure and local elemental composition of the ore sample were studied by scanning electron microscopy (SEM) and energy dispersive spectrometry (EDS) using a MIRA 3 LMU auto emission electron microscope (TESCAN) equipped with an INCA Energy 350 X-max 80 energy dispersive X-ray spectrometer (Oxford Instruments). SEM imaging was performed at an accelerating voltage of 20 kV, an electron beam current of 20 nA, and an effective beam resolution of $3\text{ }\mu\text{m}$. During the preparation of the specimen for analysis, a sample was embedded into bakelite, the surface of the cured cylindrical block was polished and coated with a thin carbon layer layer (25 nm).

Kinetic analysis of the oxidation of the ore was performed by mathematical treating of DSC heating data of its sample for three temperature programs ($\beta_i = 5, 10,$ and $20\text{ }^{\circ}\text{C}\cdot\text{min}^{-1}$) in the boundaries of exothermic and endothermic peaks corresponding to the development of this process. First, the inverse kinetic problem was solved, i.e., the kinetic parameters of oxidation were determined based on the experimental data. For this purpose, each j -th ($j = 1, 2, \dots, N$) elementary DSC peak was considered as a trace of the

j -th formal irreversible one-step reaction $A_j \rightarrow B_j$, where A_j and B_j are the initial formal reagent and the final formal product, respectively (both the complex and simple i -th curve peaks obtained by separation were counted as elementary peaks). The completion and intensity of the j -th reaction at the i -th temperature program were quantified through conversion degree (α_{ij}) and reaction rate ($d\alpha_{ij}/dt$, s^{-1}) of $A_j \rightarrow B_j$ transformation [77, 78] according to the equations:

$$\alpha_{ij} = \frac{\int_{t_{oij}}^t \left(\frac{dH_{ij}(t)}{dt}\right) dt}{\int_{t_{oij}}^{t_{eij}} \left(\frac{dH_{ij}(t)}{dt}\right) dt} = \frac{\int_{T_{oij}}^T \left(\frac{dH_{ij}(T)}{dT}\right) dT}{\int_{T_{oij}}^{T_{eij}} \left(\frac{dH_{ij}(T)}{dT}\right) dT}, \quad (1)$$

$$\frac{d\alpha_{ij}}{dt} = k_j(T) f_j(\alpha_{ij}) = A_j \exp\left(-\frac{E_j}{RT}\right) f_j(\alpha_{ij}), \quad (2)$$

where t_{oij} and t_{eij} are the initial and final moments of the reaction (that is, the moments of the beginning and the end of the deviation of the DSC curve from the baseline), respectively, s ($t_{oij} = 0\text{ s}$); t is the current reaction time, s ($t_{oij} < t < t_{eij}$); T_{oij} and T_{eij} are the temperatures of the beginning and the end of the reaction, respectively, K; T is the temperature at the current time moments of the reaction, K ($T_{oij} < T < T_{eij}$); $H_{ij}(T)$ and $H_{ij}(t)$ are the functions describing the dependence of reaction enthalpy on temperature and time, respectively, $\text{J}\cdot\text{g}^{-1}$; $k_j(T)$ is the reaction rate constant invariant with respect to the temperature program, s^{-1} ; $f_j(\alpha_{ij})$ is the reaction model invariant with respect to the temperature program (i.e. a function reflecting the reaction mechanism); E_j is the effective activation energy invariant with respect to the temperature program, $\text{J}\cdot\text{mol}^{-1}$; A_j is a pre-exponential factor invariant with respect to the temperature program, s^{-1} ; R is the gas constant, $\text{J}\cdot\text{mol}^{-1}\cdot\text{K}^{-1}$. In the calculations it was assumed that the temperature changes over time according to a linear law:

$$T = T_{oij} + \beta_i t, \quad (3)$$

and $\beta_i = dT/dt = \text{Const}$. The Johnson–Mehl–Avrami–Erofeev–Kolmogorov (JMAEK) model [78, 79] was used as the reaction model $f_j(\alpha_{ij})$ (its choice is due to the reaction model identification results described below):

$$f(\alpha_{ij}) = n_j (1 - \alpha_{ij}) \left[-\ln(1 - \alpha_{ij})\right]^{(n_j - 1)/n_j}, \quad (4)$$

which is based on the following equation describing the kinetics of nucleation and crystal growth of the new phase in the parent phase

$$\alpha_{ij} = 1 - \exp(-k_j t^{n_j}) = 1 - \exp\left[-A_j \exp\left(-\frac{E_j}{RT}\right) \left(\frac{T - T_{oij}}{\beta_i}\right)^{n_j}\right]; \quad (5)$$

here n_j is the Avrami exponent invariant with respect to the temperature program, which depends on the mechanism of the process. The initial estimation of the apparent activation energy (E_j , $\text{J}\cdot\text{mol}^{-1}$) and the pre-exponential factor (A_j , s^{-1}) was performed by the Kissinger method [78, 80]; the method is based on estimating the slope ($-E_j/R$) and

intercept ($\ln(A_j R/E_j)$) of a pairwise linear regression for the model

$$\ln\left(\frac{\beta_i}{T_{p_{ij}}^2}\right) = \ln\frac{A_j R}{E_j} - \frac{E_j}{RT_{p_{ij}}}, \quad (6)$$

constructed from the pairs of observed values of $\ln(\beta_i/T_{p_{ij}}^2)-1/T_{p_{ij}}$ for each β_i . The reliability of approximation was controlled by the value of the coefficient of determination (R_j^2). In order to identify the reaction model for the j -th reaction at the i -th temperature program, numerical values of the reference function $y_{ij}(\alpha_{ij})$ were calculated for a given series of values α_{ij} varying from 0.1 to 1 in step of 0.1:

$$y(\alpha_{ij}) = \left(\frac{d\alpha_{ij}}{dt}\right)_{\alpha_{ij}} \exp\left(\frac{E_j}{RT_{\alpha_{ij}}}\right); \quad (7)$$

then the pairs of $y_{ij}(\alpha_{ij})-\alpha_{ij}$ for each β_i were plotted on the coordinate plane and the resulting curves were compared with the theoretical plots of the function $y(\alpha)$ for the tabulated forms $f(\alpha)$. The reaction model selection was based on qualitative correspondence between the experimental and theoretical curves.

The invariant Avrami exponent (n_j) of the j -th reaction was determined by the Augis–Bennett method [81]; the calculation was performed using the formulae:

$$n_j = \frac{1}{3} \sum_{i=1}^3 n_{ij}, \quad (8)$$

$$n_{ij} = \frac{2,5RT_{p_{ij}}^2}{E_j \Delta T_{ij}}, \quad (9)$$

where n_{ij} is the Avrami exponent of the j -th reaction for the i -th heating rate; the value of E_j ($\text{J}\cdot\text{mol}^{-1}$) was taken from the Kissinger analysis. After that, the following iterations were performed: the values of invariant kinetic parameters of elementary reactions (E_j , A_j , and n_j) were substituted into equation (5), analytical expressions were found to estimate the conversion degree (α_{ij}) for each j -th reaction and i -th temperature program, calculated kinetic curves $\alpha_{ij}-T$ were reconstructed, and, by varying the parameter A_j from its initial value at fixed E_j and n_j , the obtained model was optimized by approximating experimental curves with the calculated ones (the quality of approximation at this and subsequent iterations was controlled by the value of the Pearson correlation coefficient (r_{ij})). The refined value of the invariant pre-exponential factor (A_j^r , s^{-1}) was obtained as the arithmetic mean of the optimal A_j values for all temperature programs. Then obtained A_j^r value was substituted into equation (5), the parameters A_j^r and n_j were fixed, and the model was optimized by varying E_j from its initial value to obtain a refined invariant value of the activation energy (E_j^r , $\text{J}\cdot\text{mol}^{-1}$). At the final stage of optimization, the fixed values of E_j^r and A_j^r were substituted into equation (5) and the model was optimized by varying n_j from its initial value to determine the refined invariant value of the Avrami exponent (n_j^r).

The optimum invariant kinetic parameters found were used to solve a direct kinetic problem in relation to the ore oxidation process in the studied range of temperature programs; by substituting E_j^r , A_j^r , and n_j^r values into equations (5) and (2), analytical expressions were obtained to calculate the conversion degree (α_j) and conversion rate ($d\alpha_j/dt$, s^{-1}) at for the elementary reactions. Verification of the models for each reaction was carried out by assessing the closeness of the correlation between theoretical and experimental data; for this purpose, refined calculated kinetic curves $\alpha_{ij}-T$ were suggested and compared with the experimental ones; the Pearson correlation coefficient averaged over all temperature programs (r_{avj}) served as the optimality criterion:

$$r_{avj} = \frac{1}{3} \sum_{i=1}^3 r_{ij}. \quad (10)$$

3. Results and Discussion

According to the ICP AES data, the original ore has the following composition, mass%: 0.98 Cu, 0.01 Ni, 0.10 Co, 0.78 Zn, 38.5 Fe, 30.2 S, 0.03 As, 17.0 SiO_2 , 0.9 CaO, 6.7 MgO, and 4.8 others. At the ordinary content of copper (0.98 mass%) and zinc (0.78 mass%) it is characterized by higher (0.10 mass%) content of cobalt. The approximate mass fractions of sulfides and rock-forming components are 63.3% and 36.7%, respectively. According to the XRD data (Figure 1) the total content of sulfide phases in the initial ore sample, determined by the RIR method, is 42.4 mass%; among the revealed minerals pyrite (FeS_2), chalcopyrite (CuFeS_2), and wurtzite (ZnS) can be noted, the fractions of which are 30.7, 3.1, and 8.6 mass%, respectively. There are barren minerals in the rest of the ore (57.6 mass%), such as: tremolite ($\text{Ca}_2\text{Mg}_5\text{H}_2(\text{SiO}_3)_8$), siderite (FeCO_3), and quartz (SiO_2), whose fractions are 17.1, 2.6, and 38.0 mass%, respectively.

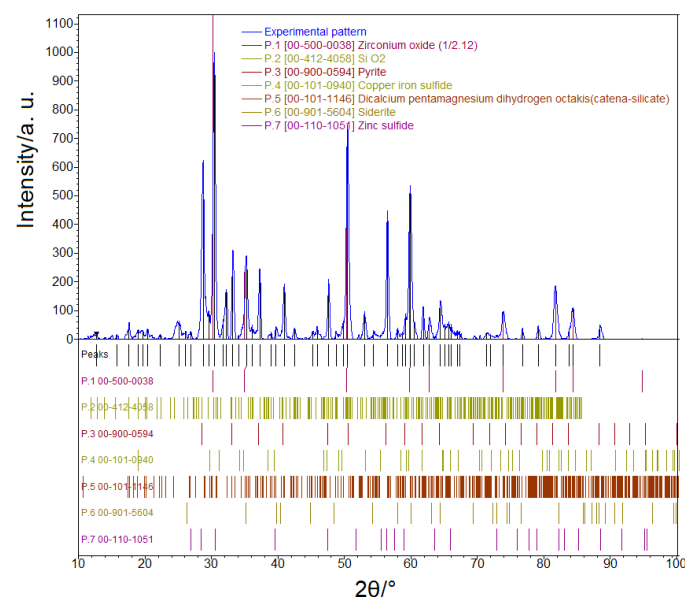


Figure 1 XRD patterns of the initial ore at 25 °C (the reflections of zirconium dioxide refer to the substrate).

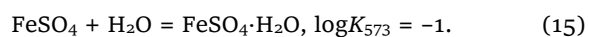
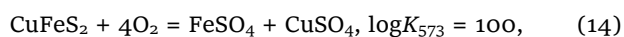
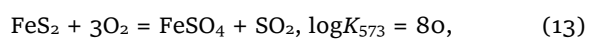
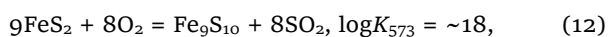
The SEM and EDS study showed that the ore has a full-crystalline porphyry-like fine-grained structure characterized by close germination of sulfide and oxide phases, and has a massive (disordered) texture. In the matrix represented by magnesium silicate, there are hydrated iron (III) oxide, and iron and calcium carbonates of the compositions $Mg_3Si_4O_{10}(OH)_2$ (talc), $Fe_2O_3 \cdot nH_2O$ (limonite), $FeCO_3$ (siderite), and $CaCO_3$ (calcite) respectively. In addition, there are distributed phenocrystals (5–150 μm) of iron sulfide corresponding in composition to pyrite (FeS_2), and small (up to 5 μm) inclusions with sphalerite ($Zn_{1-x}Fe_xS$) and chalcopyrite ($CuFeS_2$) formulae.

The data on the composition and structure of the ore obtained by XRD, SEM, and EDS methods complement each other and satisfactorily agree with the data obtained earlier for the ore of the same deposit [3, 4]. Summarizing the data obtained in the present work, we can conclude that the main ore minerals of the studied sample may be pyrite, pyrrhotite, chalcopyrite, sphalerite (wurtzite), and limonite, and the barren minerals are tremolite, silica, talc, siderite, calcite, and some iron aluminosilicates. Regarding the distribution of non-ferrous metals, it should be noted that, in contrast to copper and zinc, cobalt does not form its own mineral forms, and in the amount up to 0.35 mass% it is isomorphically included in pyrite.

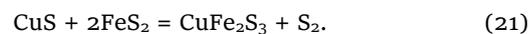
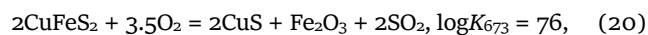
It follows from the HTXRD data that there were no significant changes in the phase composition of the initial sample before 200 °C; only at 200 °C the appearance of iron (III) sulfate ($Fe_2(SO_4)_3$) was noted, indicating the beginning of pyrite oxidation by the following reaction:



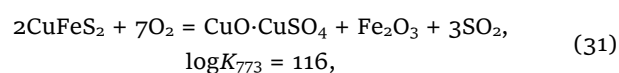
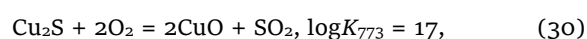
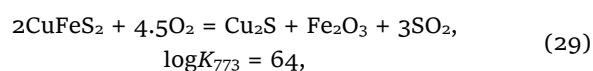
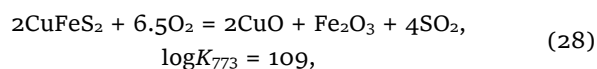
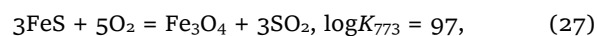
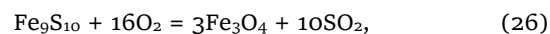
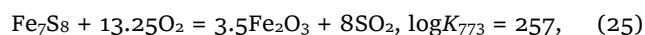
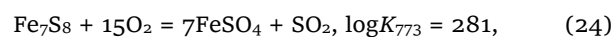
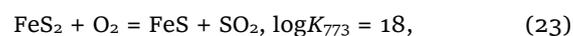
The fact of low-temperature pyrite oxidation agrees with the data [15, 52]. The formation of hexagonal pyrrhotite (Fe_9S_{10}), poitevinite ($FeSO_4 \cdot H_2O$), and copper (II) sulfate ($CuSO_4$) at 300 °C can be associated with the processes described by the following equations:



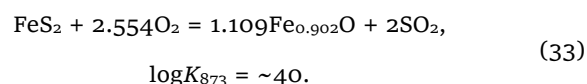
In this case, the reason for the appearance of hydrate compounds may be the interaction of oxidation products with water contained in the air, released during the dehydration of rock-forming minerals. At 400 °C, in addition to the phases formed at 300 °C, monoclinic pyrrhotite (Fe_7S_8), cubanite ($CuFe_2S_3$), magnetite (Fe_3O_4), and hematite (Fe_2O_3) were detected, formed by the reactions listed below [15]:



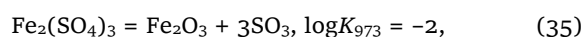
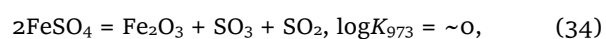
Despite the fact that the presence of pyrite in the roasting product at 400 °C was not confirmed, its reflections reappear at 500 °C; the other newly formed phases are hexagonal modifications of iron sulfide with the formulae of $Fe_{11}S_{12}$ and FeS , dolerophanite ($CuO \cdot CuSO_4$), and tenorite (CuO); in this regard the oxidation chemistry can be supplemented with the following set of equations [15, 50]:

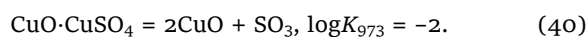
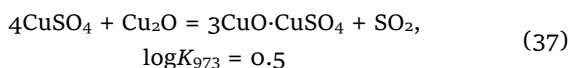


Reaching 600 °C is characterized by the complete consumption of iron and copper sulfides with the formation of hematite and magnetite, iron (II) and (III) and copper (II) sulfates according to reactions (13), (14), (24)–(30), and also by the appearance of wustite ($Fe_{0.902}O$), which is formed according to the reaction:

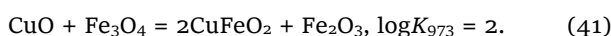


Starting from 700 °C, the products of roasting show the absence of sulfates, which is associated their decomposition [15, 20, 27, 31–33, 50, 52, 82]:

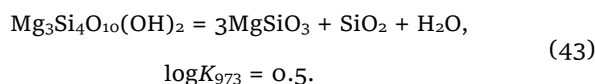
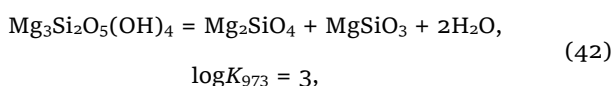




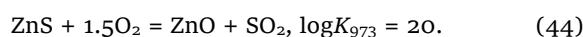
The products of sulfide oxidation in this case are wustite, magnetite and hematite, as well as copper (I) ferrite (CuFeO₂), which appears as a result of the attack of magnetite on copper (II) oxide:



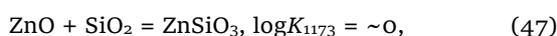
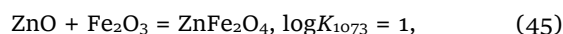
At the same temperature, one can expect the onset of intensive thermal decomposition of hydrated magnesium silicates, for example, chrysotile (Mg₃Si₂O₅(OH)₄) and talc (Mg₃Si₄O₁₀(OH)₂), leading to the formation of metasilicates, in particular diopside (CaFe_{0.13}Mg_{0.943}Si_{1.927}O₆); these processes can be represented by a general scheme [83]:



The absence of traces of forsterite (Mg₂SiO₄) in the corresponding diffractograms may be due to its amorphousness at the initial moments of formation. Also, at 700 °C, reflections from zincite (ZnO) formed according to the following equation were detected [29]:



At 800 and 900 °C, the final products of deep roasting are formed containing hematite (Fe₂O₃), magnetite (Fe₃O₄), and diopside (Fe_{0.015}Mg_{0.985}SiO₃ at 800 °C and Fe_{0.15}Mg_{1.82}Si₂O₆ at 900 °C), which originate in the above reactions. At 800 °C, franklinite (ZnFe₂O₄) and copper ferrite of the composition CuFe₅O₈ can additionally be formed, and at 900 °C – zinc silicate (ZnSiO₃), tenorite (CuO), and delafossite (CuFeO₂); the first three of these phases are the products of the following reactions [29, 63, 84]:



Where the last two are the processes described by equations (28) and (41). The composition of the gas phase in the considered temperature range is determined by the reaction



whose direction changes from direct to reverse at ~780 °C. It should also be noted that the absence of siderite and zinc sulfide reflections in a number of diffractograms in the temperature ranges of their possible existence can be explained by the low sensitivity of the applied analytical method with respect to these phases. The values of the equilibrium constants of most of the listed reactions exceed (or are close to) unity, which confirms the possibility of their proceeding in the forward direction (reactions for which, due to the lack of thermodynamic data for a number of compounds in the HSC Chemistry 6.12 package, the *K_T* value is not indicated, are hypothetical or confirmed by literature data). On the whole, the presented reactions can only serve as the simplest explanation for the appearance of phases detected by XRD in the roasting products; it is obvious that the chemistry of the ore oxidation is even more complex.

The results of thermal analysis of the ore carried out under heating conditions from 30 to 1100 °C in air flow (30 cm³·min⁻¹) with heating rates of β_i = 5, 10, and 20 °C·min⁻¹ is presented in Figures 2 and 3, and Table 1. There are three primary thermal effects on the DSC curves (Figure 2). The first effect is a complex exothermic peak of high intensity formed by a series of partially overlapping (partially resolved at β_i = 5 °C·min⁻¹) elementary exothermic peaks. The separation of complex exothermic peaks showed (Figure 3 and Table 1) that each of them is the result of the superimposition of five elementary exothermic peaks (hereinafter referred to as EP₁, EP₂, EP₃, EP₄, and EP₅). The second and third effects are weakly expressed simple (elementary) endothermic peaks (hereinafter referred to as EP₆ and EP₇).

According to the TG data (Figure 2), by 1100 °C the total mass loss during oxidation is 28–29%, of which the 30–318 °C region free of DSC effects accounts for 4–5%, and the series of exothermic (359–570 °C) and two endothermic (561–664 °C and 743–927 °C) anomalies are 7–10, 8–9, and 4–6% respectively; the remaining losses account for the high-temperature region.

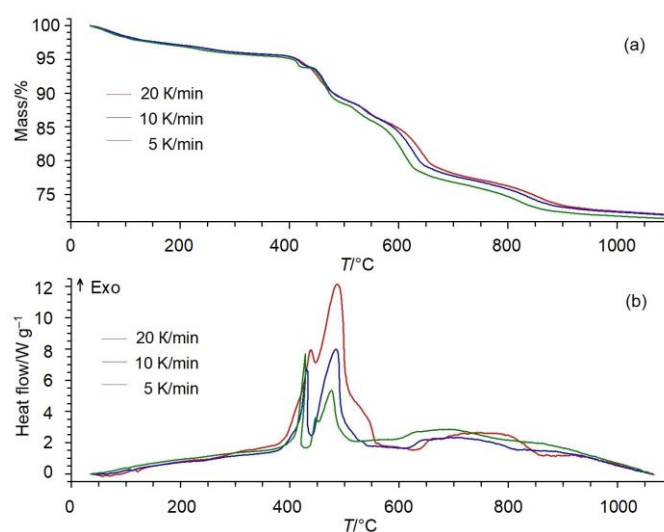


Figure 2 TG and DSC curves (β_i = 5, 10, and 20 °C·min⁻¹) for the pyritic copper ore.

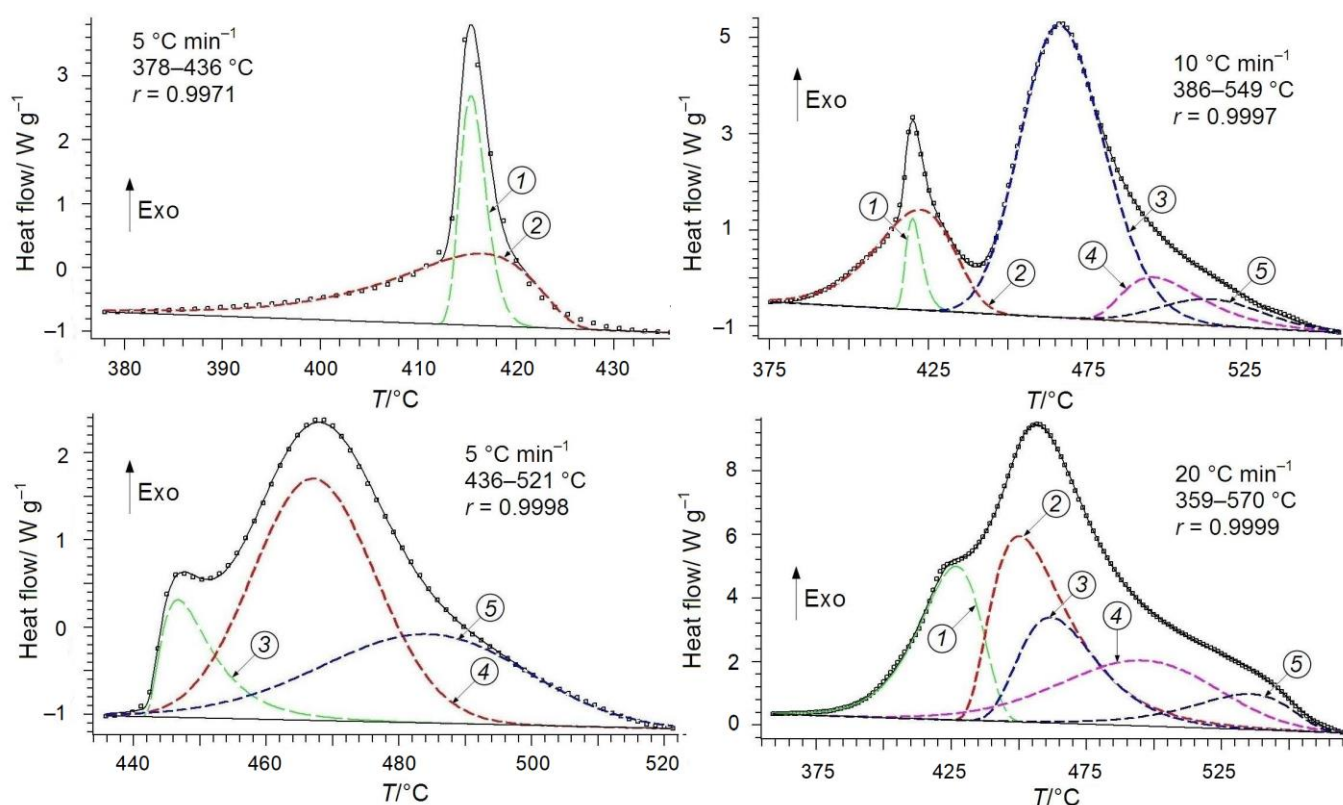


Figure 3 Separation results for complex exothermic DSC peaks. Solid straight lines are baselines, dots are experimental DSC data, dashed curves are calculated DSC curves for elementary peaks, and solid curves are summary calculated DSC curves. The circles with arrows show the numbers of elementary peaks.

Table 1 Parameters of the elementary DSC peaks, and n_{ij} values calculated by the Augis–Bennett method.

Parameter	Value						
	$\beta_i = 5 \text{ }^\circ\text{C}\cdot\text{min}^{-1}$						
Peak	EP1	EP2	EP3	EP4	EP5	EP6	EP7
$T_{oij}/^\circ\text{C}$	413	397	442	449	451	561	743
$T_{pij}/^\circ\text{C}$	415	417	447	467	484	598	774
$T_{eij}/^\circ\text{C}$	418	426	457	486	514	629	834
$\Delta T_{pij}/\text{K}$	3.1	16.3	12.6	23.8	14.0	32.2	43.5
n_{ij}	2.5	1.6	1.5	1.2	2.8	1.8	3.4
	$\beta_i = 10 \text{ }^\circ\text{C}\cdot\text{min}^{-1}$						
Peak	EP1	EP2	EP3	EP4	EP5	EP6	EP7
$T_{oij}/^\circ\text{C}$	416	394	442	478	483	566	760
$T_{pij}/^\circ\text{C}$	420	422	466	496	513	615	814
$T_{eij}/^\circ\text{C}$	426	443	494	527	546	645	867
$\Delta T_{pij}/\text{K}$	5.7	28.7	30.8	27.9	37.1	38.3	33.6
n_{ij}	1.4	0.9	0.7	1.2	1.2	1.6	4.7
	$\beta_i = 20 \text{ }^\circ\text{C}\cdot\text{min}^{-1}$						
Peak	EP1	EP2	EP3	EP4	EP5	EP6	EP7
$T_{oij}/^\circ\text{C}$	398	431	440	433	489	596	798
$T_{pij}/^\circ\text{C}$	427	450	462	496	536	630	855
$T_{eij}/^\circ\text{C}$	445	488	498	549	562	664	927
$\Delta T_{pij}/\text{K}$	26.8	31.9	33.9	38.1	42.4	31.4	42.5
n_{ij}	0.3	0.9	0.6	0.8	1.1	1.8	4.0

Theoretical calculations demonstrated that the removal of all volatile components (H_2O , CO_2 , and S) into the gas phase should reduce the mass of the sample by $\sim 20\%$; the experimental estimate exceeds this value, indicating either a possible error in determining the material composition of the ore or a more complex process.

The zone of exothermic processes is confined to the traces of intense gas emission noted on the MS curves

(Figure 4): SO_2 ($T_p^{\text{SO}_2} = 415$ and $466 \text{ }^\circ\text{C}$ at $\beta_i = 5 \text{ }^\circ\text{C}\cdot\text{min}^{-1}$, $T_p^{\text{SO}_2} = 420$ and $465 \text{ }^\circ\text{C}$ at $\beta_i = 10 \text{ }^\circ\text{C}\cdot\text{min}^{-1}$, and $T_p^{\text{SO}_2} = 427$ and $456 \text{ }^\circ\text{C}$ at $\beta_i = 20 \text{ }^\circ\text{C}\cdot\text{min}^{-1}$), SO_3 ($T_p^{\text{SO}_3} = 415 \text{ }^\circ\text{C}$ and $464 \text{ }^\circ\text{C}$ at $\beta_i = 5 \text{ }^\circ\text{C}\cdot\text{min}^{-1}$, $T_p^{\text{SO}_3} = 419$ and $472 \text{ }^\circ\text{C}$ at $\beta_i = 10 \text{ }^\circ\text{C}\cdot\text{min}^{-1}$, and $T_p^{\text{SO}_3} = 463 \text{ }^\circ\text{C}$ at $\beta_i = 20 \text{ }^\circ\text{C}\cdot\text{min}^{-1}$), and CO_2 ($T_p^{\text{CO}_2} = 519 \text{ }^\circ\text{C}$ at $\beta_i = 5 \text{ }^\circ\text{C}\cdot\text{min}^{-1}$, $T_p^{\text{CO}_2} = 536 \text{ }^\circ\text{C}$ at $\beta_i = 10 \text{ }^\circ\text{C}\cdot\text{min}^{-1}$, and $T_p^{\text{CO}_2} = 546 \text{ }^\circ\text{C}$ at $\beta_i = 20 \text{ }^\circ\text{C}\cdot\text{min}^{-1}$).

Subsequent endothermic events are associated with peaks in the SO₂ ion current ($T_p^{SO_2} = 604$ and 819 °C at $\beta_i = 5$ °C·min⁻¹, $T_p^{SO_2} = 632$ and 842 °C at $\beta_i = 10$ °C·min⁻¹, and $T_p^{SO_2} = 647$ and 855 °C at $\beta_i = 20$ °C·min⁻¹). The MS traces also revealed three weak peaks of the ion current of water, the maxima of which ($T_p^{H_2O}$) vary in the ranges of 120–125, 290–310, and 950–960 °C.

Analysis of the results of HTXRD, DSC, TG, and MS shows that heating ($\beta_i = 5$ – 20 °C·min⁻¹) of the pyritic copper ore up to 318 °C is accompanied by the removal of adsorption (capillary) and hygroscopic moisture into the gas phase, which is associated with the initial monotonic mass loss ($\Delta m = 4$ – 5%) and the release of the H₂O into the gas phase at 120–125 and 290–310 °C. The main oxidation period of pyritic copper ore, associated with the release of the largest ($-\Delta H = 1468$ – 2052 J·g⁻¹) amount of heat, begins at 359 °C, culminates at 420–468 °C, and finished at 570 °C; it accounts for up to ~34 relative % total mass loss.

Numerous interactions of the ore minerals with a gaseous atmosphere can occur within its boundaries, described by equations (12)–(32); some reactions are characterized by a high thermal effect and provide for the release of a large amount of SO₂ capable of interacting with O₂ by reaction (48). The appearance of CO₂, intensifying at 519–546 °C, can be associated with the oxidative decomposition of siderite:



Based on the fact of the absence of mass increase revealed by the TG method, the main processes in this temperature range can be associated with ignition and direct oxidation (burning) of sulfides with the formation of oxides [15]; the formation of sulfates is limited, or they are effectively broken by sulfide compounds. The final stage of the oxidation includes two processes accompanied by weak endothermic effects ($\Delta H = 49$ – 97 and 51 – 113 J·g⁻¹, respectively), mass reduction (up to ~31 and ~21 relative %, respectively), and SO₂ release; apparently, in this case, thermal decomposition of residual sulfates takes place: iron sulfates at 561–664 °C (reactions (34) and (35)) and copper sulfates at 743–927 °C (reactions (39) and (40)). This conclusion is confirmed by the literature data [19, 31, 57, 86, 87]. At 950–960 °C, part of the crystallization water of rock-forming silicate minerals is released.

Thus, the kinetics of oxidative roasting of the ore can be formally attributed to seven elementary reactions: five exothermic (at 398–445, 394–488, 440–498, 433–549, and 451–562 °C) corresponding to intensive burning of iron, copper and zinc sulfides, and two endothermic (at 561–664 °C and 743–927 °C) related to the decomposition of residual copper and iron sulfates. The grouped DSC peaks of the same name, which are their traces, are shown in Figure 5. The results of kinetic analysis of the DSC data in relation to the temperature ranges of these reactions are presented in Figures 6, and 7, and Table 2.

The shape of the plots of the $y_{ij}(\alpha_{ij})$ function (Figure 7) for elementary oxidation reactions corresponds to the JMAEK (An) kinetic model of nucleation and crystal growth [78].

The refined invariant kinetic parameters of the elementary reactions differ somewhat from the initial estimates (Table 2).

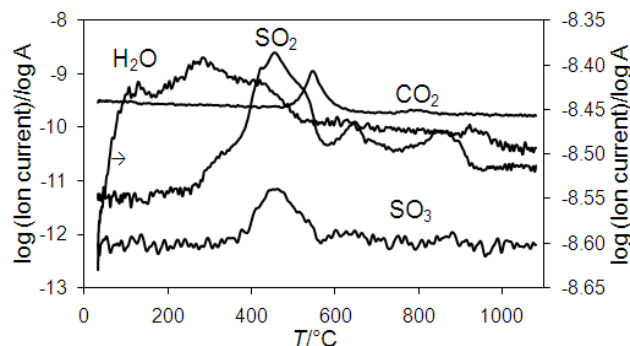


Figure 4 MS curves ($\beta_i = 20$ °C·min⁻¹) for the pyritic copper ore.

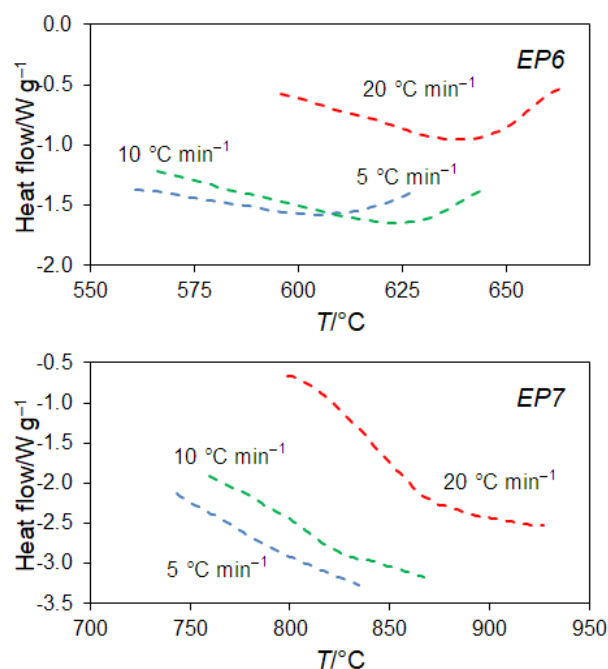


Figure 5 Grouping results for elementary endothermic DSC peaks (Results for exothermic elementary DSC peaks have a similar view).

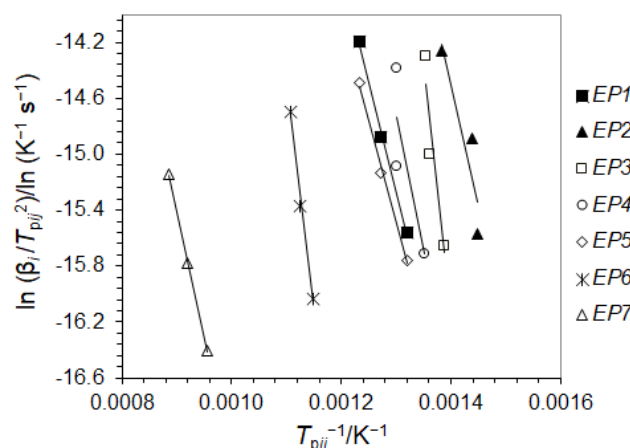


Figure 6 Kissinger plots for elementary DSC peaks.

The kinetic models derived from these parameters have the following form:

$$\frac{d\alpha_1}{dt} = 4.89 \cdot 10^{31} \exp\left(-\frac{459000}{RT}\right) (1 - \alpha_1) [-\ln(1 - \alpha_1)]^{0.29}, \quad (50)$$

$$\frac{d\alpha_2}{dt} = 4.52 \cdot 10^8 \exp\left(-\frac{140000}{RT}\right) (1 - \alpha_2) [-\ln(1 - \alpha_2)]^{0.09}, \quad (51)$$

$$\frac{d\alpha_3}{dt} = 4.74 \cdot 10^{13} \exp\left(-\frac{220000}{RT}\right) (1 - \alpha_3), \quad (52)$$

$$\frac{d\alpha_4}{dt} = 1.32 \cdot 10^8 \exp\left(-\frac{160000}{RT}\right) (1 - \alpha_4) [-\ln(1 - \alpha_4)]^{0.09}, \quad (53)$$

$$\frac{d\alpha_5}{dt} = 1.24 \cdot 10^6 \exp\left(-\frac{155000}{RT}\right) (1 - \alpha_5) [-\ln(1 - \alpha_5)]^{0.41}, \quad (54)$$

$$\frac{d\alpha_6}{dt} = 5.88 \cdot 10^{15} \exp\left(-\frac{320000}{RT}\right) (1 - \alpha_6) [-\ln(1 - \alpha_6)]^{0.17}, \quad (55)$$

$$\frac{d\alpha_7}{dt} = 1.69 \cdot 10^4 \exp\left(-\frac{149000}{RT}\right) (1 - \alpha_7) [-\ln(1 - \alpha_7)]^{0.17}, \quad (56)$$

Verification of the obtained models showed a high ($r_{avj} = 0.8580-0.9984$) level of correlation between the refined calculated and experimental data (Figure 8, and Table 2). Therefore, these models describe the kinetic patterns of oxidation of the investigated pyritic copper ore under given conditions with sufficient reliability.

According to the literature data, the effective activation energy of the processes accompanying the oxidation (when heated in air) of iron, copper, and zinc sulfides, as well as their natural and artificial mixtures of various sizes (from -0.043 to -12 mm), can be of $7-463$ $\text{kJ}\cdot\text{mol}^{-1}$ [11, 14, 19, 26, 27, 40, 41, 53, 60, 67, 69, 72, 82, 85]; the estimates obtained in this work ($E_j^r = 124-455$ $\text{kJ}\cdot\text{mol}^{-1}$) do not go beyond this range. The results of determining the reaction model show that the limiting step of all elementary oxidation reactions of the studied ore is nucleation and crystal growth. The examples of the application of the JMAEK model to describe the mechanism of oxidation of sulfides (in particular, chalcopyrite and pyrite concentrates) should be mentioned [41, 67, 88]. The values of the Avrami exponent (n_j^r) obtained in this work are in the range from 1 to 1.7, which allows us to draw the following conclusions regarding the details of the mechanism and morphological features of the process: i) crystallization of the products of elementary reactions is accompanied by an increase in the number of nuclei;

ii) nuclei of a new phase may be formed both at the interface and in the volume of the ore particles; iii) crystal growth is one-dimensional and controlled by a chemical reaction at the phase boundary or diffusion of reagents [89].

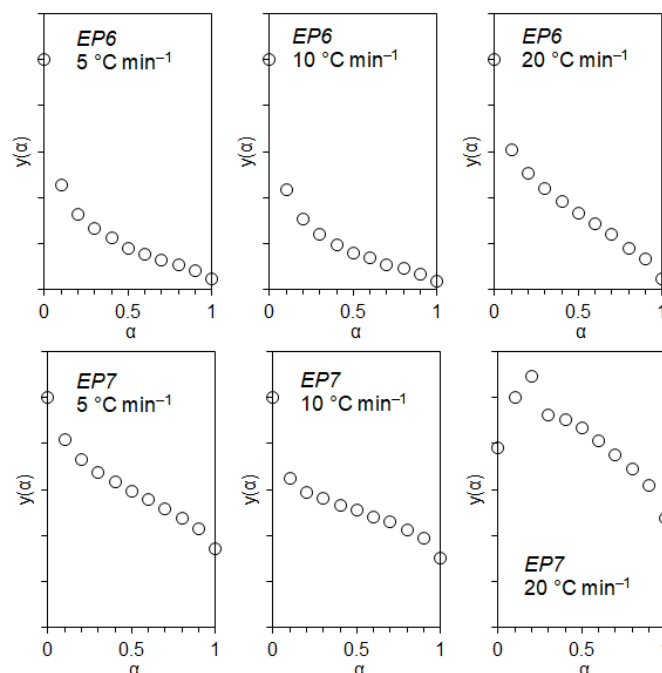


Figure 7 Master plots $y(\alpha)$ for endothermic elementary reactions (Results for exothermic elementary reactions have a similar view).

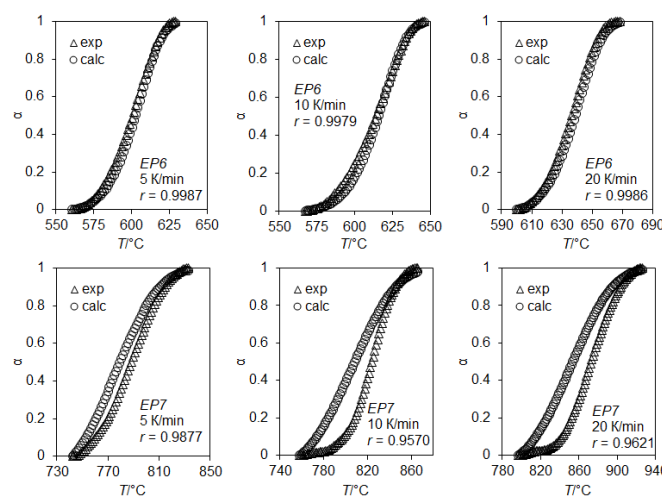


Figure 8 Experimental (circles) and refined calculated (triangles) kinetic curves for endothermic elementary reactions (Results for exothermic elementary reactions have a similar view).

Table 2 Kinetic parameters of elementary reactions.

Elementary reaction	Kinetic parameter						
	$E_j/\text{kJ}\cdot\text{mol}^{-1}$	$E_j^r/\text{kJ}\cdot\text{mol}^{-1}$	$\log A_j/\log(\text{s}^{-1})$	$\log A_j^r/\log(\text{s}^{-1})$	n_j	n_j^r	r_{avj}
1	455±22	459	32.5	31.5	1.4	1.4	0.8615
2	142±21	140	8.3	8.6	1.1	1.1	0.8580
3	220±22	220	13.7	13.7	1.0	1.0	0.9464
4	159±21	160	8.7	8.1	1.1	1.1	0.9527
5	124±20	155	5.9	5.9	1.7	1.7	0.9928
6	275±15	320	15.6	15.7	1.7	1.2	0.9984
7	154±14	149	4.4	4.2	4.0	1.2	0.9689

Note. The numbers of elementary reactions correspond to the numbers of elementary peaks in Table 1.

It should be noted that, compared with copper concentrates, pyritic copper ore is a material that is more technologically complex, and the purpose of its roasting is not only the removal of a certain amount of sulfur into the gas phase, but also the corresponding transformation (decomposition and dehydration) of rock-forming minerals.

4. Limitations

For deeper understanding of the kinetics of solid-state oxidation of the studied sulfide systems, it is necessary to verify the data obtained in this work with the results of studying the isothermal kinetics of the process and information about the microstructure of the oxidation products.

5. Conclusions

The formal kinetics of the solid-state oxidation of iron, copper and zinc sulfide natural mixture, typical of the pyritic copper ores, can be attributed to seven elementary reactions: five exothermic (at 398–445, 394–488, 440–498, 433–549, and 451–562 °C), corresponding to intensive burning of iron, copper and zinc sulfides, and two endothermic (at 561–664 and 743–927 °C), related to the decomposition of residual copper and iron sulfates.

The limiting steps of these reactions are nucleation and crystal growth, and the values of activation energy, pre-exponential factor and Avrami exponent are in the ranges of 140–459 kJ·mol⁻¹, 1.41·10⁴–3.49·10³¹ s⁻¹, and 1.0–1.7, respectively. Crystallization of the products of elementary reactions is accompanied by an increase in the number of nuclei; nuclei of a new phase may be formed both at the interface and in the volume of the ore particles, and crystal growth is one-dimensional and controlled by a chemical reaction at the phase boundary or diffusion.

The resulting kinetic models make it possible to predict a degree of process completion depending on time and temperature. The results of the work as a whole can contribute to the development of theoretical ideas about the physico-chemical transformations of pyrite ores and concentrates during pyrometallurgical operations, and can also be used in the practice of oxidative roasting of these materials.

• Supplementary materials

No supplementary materials are available.

• Funding

This research had no external funding.

• Acknowledgments

The work was carried out according to the State Assignment for IMET UB RAS (No. 122020100404-2) using equipment of the Collaborative usage center "Ural-M".

• Author contributions

Conceptualization: A.M.K.

Methodology: A.M.K.

Formal analysis: A.M.K.

Investigation: R.I.G. and S.M.P.

Writing – original draft preparation: A.M.K.

Writing – review and editing: R.I.G.

• Conflict of interest

The authors declare no conflict of interest.

• Additional information

Author IDs:

Alexander M. Klyushnikov, Scopus ID [57220987625](#);

Sergey M. Pikalov, Scopus ID [6603186623](#);

Roza I. Gulyaeva, Scopus ID [6602478183](#).

Website:

Institute of Metallurgy of the Ural Branch of the Russian Academy of Sciences, <http://www.imet-uran.ru>.

References

- Schlesinger ME, King MJ, Sole KC, Davenport WG. Extractive Metallurgy of Copper. 5th Edition. Oxford: Elsevier; 2011.
- Selivanov EN, Gulyaeva RI, Klyushnikov AM. Study of structure and phase composition of copper-cobalt sulfide ores of Dergamyshskoe deposit. Tsvetnye Metally. 2016;3:13–17. doi:[10.17580/tsm.2016.03.02](#)
- Melekestseva IYu, Maslennikova VV, Maslennikova SP. Trace elements in sulfides of the Dergamysh cobalt-bearing massive sulfide deposit, the Southern Urals: Mode of occurrence and matter sources. Lithosphere (Russia). 2020;20(4):499–516. doi:[10.24930/1681-9004-2020-20-4-499-516](#)
- Nagaeva SP, Mezentseva OP, Kozorez MV. Mineralogical researches of copper cobalt-containing ores of Dergamysh deposit. Gornyi Zhurnal/Mining J. 2014;11:31–4.
- Cusano G, Gonzalo MR, Farrell F, Remus R, Roudier S, Delgado Sancho L. Best Available Techniques (BAT) Reference Document for the main Non-Ferrous Metals Industries, EUR 28648 EN, 902–910.
- Reznik ID, Sobol SI, Khudyakov VM. Cobalt. Vol. 1. Moscow: Mashinostroyeniye; 1995 (In Russian).
- Crundwell FK, Moats MS, Ramachandran V, Robinson TG, Davenport WG. Extractive metallurgy of nickel, cobalt and platinum-group metals. Oxford: Elsevier; 2011.
- Warner AEM, Diaz CM, Dalvi AD, Mackey PJ, Tarasov AV, Jones RT. JOM world nonferrous smelter survey part IV: nickel: sulfide. JOM. 2007;59:58–72. doi:[10.1007/s11837-007-0056-x](#)
- Selivanov EN, Klyushnikov AM, Gulyaeva RI. Use of quartz-containing materials as fluxes in copper smelting production. Metallurgist. 2017;61(1–2):155–161. doi:[10.1007/s11015-017-0469-x](#)
- Selivanov EN, Klyushnikov AM, Gulyaeva RI. Application of sulfide copper ores oxidizing roasting products as sulfidizing agent during melting nickel raw materials to matte. Metallurgist. 2019;63(7–8):867–887. doi:[10.1007/s11015-019-00901-z](#)
- Klyushnikov AM, Gulyaeva RI, Selivanov EN, Pikalov SM. Kinetics and mechanism of oxidation for nickel-containing pyrrhotite tailings. Int J Miner Metall Mater. 2021;28(9):1469–1477. doi:[10.1007/s12613-020-2109-x](#)

12. Klyushnikov A, Gulyaeva R, Pikalov S. Cold crystallization kinetics of slag from the joint smelting of oxidized nickel and sulfide copper ores. *J Therm Anal Calorim.* 2022;147:12165–12176. doi:[10.1007/s10973-022-11429-x](https://doi.org/10.1007/s10973-022-11429-x)
13. Klyushnikov AM. Modeling of exchange interactions in melts formed during joint smelting of oxidized nickel ores and pyrrhotite concentrates. *Metallurgist.* 2022;66(1–2):190–199. doi:[10.1007/s11015-022-01314-1](https://doi.org/10.1007/s11015-022-01314-1)
14. Božinović K, Štrbac N, Mitovski A, Sokić M, Minić D, Marković B, Stojanović J. Thermal decomposition and kinetics of pentlandite-bearing ore oxidation in the air atmosphere. *Metals.* 2021;11:1364. doi:[10.3390/met11091364](https://doi.org/10.3390/met11091364)
15. Smirnov VI, Tikhonov AI. Obzhig mednyh rud i koncentratov (teoriya i praktika) (roasting of copper ores and concentrates (Theory and Practice)). Moscow: Metallurgiya; 1966.
16. Devia M, Wilkomirsky I, Parra R. Roasting kinetics of high-arsenic copper concentrates: a review. *Miner Metall Process.* 2012;29(2):121–128. doi:[10.1007/BF03402403](https://doi.org/10.1007/BF03402403)
17. Dimitrov R, Boyanov B. Investigation of the oxidation of metal sulphides and sulphide concentrates *Thermochim Acta.* 1983;64:27–37.
18. Hua Yixin, Cai Chaojun, Cui Yan. Microwave-enhanced roasting of copper sulfide concentrate in the presence of CaCO₃. *Sep Purif Technol.* 2006;50:22–29. doi:[10.1016/j.seppur.2005.11.003](https://doi.org/10.1016/j.seppur.2005.11.003)
19. Mitovski A, Štrbac N, Mihajlovic I, Sokić M, Stojanović J. Thermodynamic and kinetic analysis of the polymetallic copper concentrate oxidation process. *J Therm Anal Calorim.* 2014;118:1277–1285. doi:[10.1007/s10973-014-3838-8](https://doi.org/10.1007/s10973-014-3838-8)
20. Prasad S, Pandey BD. Thermoanalytical studies on copper-iron sulphides. *J Therm Anal Calorim.* 1999;58:625–637. doi:[10.1023/A:1010108729034](https://doi.org/10.1023/A:1010108729034)
21. Prasad PN, Lennartsson A, Samuelsson C. A mineralogical investigation of sintering in Cu-rich polymetallic concentrates during roasting in inert atmosphere. *Metall Mater Trans B.* 2020;51:1446–1459. doi:[10.1007/s11663-020-01850-8](https://doi.org/10.1007/s11663-020-01850-8)
22. Shamsuddin M, Sohn HY. Constitutive topics in physical chemistry of high-temperature nonferrous metallurgy – a review: part 1. Sulfide roasting and smelting. *JOM.* 2019;71(9):3253–3265. doi:[10.1007/s11837-019-03620-7](https://doi.org/10.1007/s11837-019-03620-7)
23. Souza R, Queiroz C, Brant J, Brocchi E. Pyrometallurgical processing of a low copper content concentrate based on a thermodynamic assessment. *Miner Eng.* 2019;130:156–164. doi:[10.1016/j.mineng.2018.10.015](https://doi.org/10.1016/j.mineng.2018.10.015)
24. Wan X, Shi J, Taskinen P, Jokilaakso A. Extraction of copper from copper-bearing materials by sulfation roasting with SO₂-O₂ gas. *JOM.* 2020;72:3436–3446. doi:[10.1007/s11837-020-04300-7](https://doi.org/10.1007/s11837-020-04300-7)
25. Wilkomirsky I, Parra R, Parada F, Balladares E, Seguel E, Etcheverry J, Díaz R. Thermodynamic and kinetic mechanisms of bornite/chalcocopyrite/magnetite formation during partial roasting of high-arsenic copper concentrates. *Metall Mater Trans B.* 2020;51:1540–1551. doi:[10.1007/s11663-020-01870-4](https://doi.org/10.1007/s11663-020-01870-4)
26. Yang F, Wu C, Cui Y, Lu G. Apparent activation energy for spontaneous combustion of sulfide concentrates in storage yard. *Trans Nonferrous Metals Soc China.* 2011;21(2):395–401. doi:[10.1016/S1003-6326\(11\)60727-9](https://doi.org/10.1016/S1003-6326(11)60727-9)
27. Živcović Ž, Mitevska N, Savović V. Kinetics and mechanism of the chalcocopyrite-pyrite concentrate oxidation process. *Thermochim Acta.* 1996;282–283:121–130. doi:[10.1016/0040-6031\(96\)02883-3](https://doi.org/10.1016/0040-6031(96)02883-3)
28. Chen TT, Dutrizac JE. Mineralogical changes occurring during the fluid-bed roasting of zinc sulfide concentrates. *JOM.* 2004;56:46–51. doi:[10.1007/s11837-004-0235-y](https://doi.org/10.1007/s11837-004-0235-y)
29. Snurnikov AP. *Gidrometallurgiya cinka (Hydrometallurgy of zinc)*. Moscow: Metallurgiya; 1981 (In Russian).
30. Dunn JG, Jayaweera SAA. Effect of heating rate on the TG curve during the oxidation of nickel sulphide concentrates. *Thermochim Acta.* 1983;61:313–317.
31. Yu D, Utigard TA. TG/DTA Study on the Oxidation of Nickel Concentrate. *Thermochim Acta.* 2012;533:56–65. doi:[10.1016/j.tca.2012.01.017](https://doi.org/10.1016/j.tca.2012.01.017)
32. Thoumsin FJ, Coussement R. Fluid-bed roasting reactions of copper and cobalt sulfide concentrates. *JOM.* 1964;16:831–834. doi:[10.1007/BF03378299](https://doi.org/10.1007/BF03378299)
33. Hu G, Dam-Johansen K, Wedel S, Hansen JP. Decomposition and oxidation of pyrite. *Prog Energy Combust Sci.* 2006;32:295–314. doi:[10.1016/J.PECS.2005.11.004](https://doi.org/10.1016/J.PECS.2005.11.004)
34. Dunn JG, Mackey LC. The measurement of ignition temperatures and extents of reaction on iron and iron-nickel sulfides. *J Therm Anal.* 1991;37:2143–2164. doi:[10.1007/BF01905584](https://doi.org/10.1007/BF01905584)
35. Luganov VA, Shabalin VI. Thermal dissociation of pyrite during processing of pyrite-containing raw materials. *Can Metall Q.* 1994;33(3):169–174. doi:[10.1179/cmq.1994.33.3.169](https://doi.org/10.1179/cmq.1994.33.3.169)
36. Dunn JG. The oxidation of sulphide minerals. *Thermochim Acta.* 1997;300:127–139. doi:[10.1016/S0040-6031\(96\)03132-2](https://doi.org/10.1016/S0040-6031(96)03132-2)
37. Eneroth E, Koch CB. Crystallite size of haematite from thermal oxidation of pyrite and marcasite – effects of grain size and iron disulphide polymorph. *Miner Eng.* 2003;16:1257–1267. doi:[10.1016/j.mineng.2003.07.004](https://doi.org/10.1016/j.mineng.2003.07.004)
38. Ferrow EA, Mannerstrand M, Sjöberg B. Reaction kinetics and oxidation mechanisms of the conversion of pyrite to ferrous sulphate: a Mössbauer spectroscopy study. *Hyperfine Interact.* 2005;163:10919. doi:[10.1007/s10751-005-9200-6](https://doi.org/10.1007/s10751-005-9200-6)
39. Aylmore MG, Lincoln F. Mechanochemical milling-induced reactions between gases and sulfide minerals. I. Reactions of SO₂ with arsenopyrite, pyrrhotite and pyrite. *J Alloys Compd.* 2000;309:61–74. doi:[10.1016/S0925-8388\(00\)00916-6](https://doi.org/10.1016/S0925-8388(00)00916-6)
40. Vázquez E, Moreno-Ventas I, Raposo I, Palma A, Díaz MJ. Kinetic of pyrite thermal degradation under oxidative environment. *J Therm Anal Calorim.* 2020;141:1157–1163. doi:[10.1007/s10973-019-09098-4](https://doi.org/10.1007/s10973-019-09098-4)
41. Ruan S, Wang C, Jie X, Yin F, Zhang Y, Yao Z, Chen Y. Kinetics of pyrite multi-step thermal decomposition in refractory gold sulphide concentrates. *J Therm Anal Calorim.* 2022;147:3689–3702. doi:[10.1007/s10973-021-10761-y](https://doi.org/10.1007/s10973-021-10761-y)
42. Wang L, Fan BW, He YT, Li P, Yin DQ, Hu YH. Characteristics of minerals and their associations of transformation processes in pyrite at elevated temperatures: an X-ray diffraction study. *Ironmaking Steelmaking.* 2014;41(2):147–152. doi:[10.1179/1743281213Y.0000000113](https://doi.org/10.1179/1743281213Y.0000000113)
43. Xu H, Guo X, Seaman LA, Harrison AJ, Obrey SJ, Page K. Thermal desulfurization of pyrite: An in situ high-T neutron diffraction and DTA-TGA study. *J Mater Res.* 2019;34:3243–3253. doi:[10.1557/jmr.2019.185](https://doi.org/10.1557/jmr.2019.185)
44. Zhang Y, Li Q, Liu X, Xu B, Yang Y, Jiang T. A thermodynamic analysis on the roasting of pyrite. *Mineral.* 2019;9:220. doi:[10.3390/min9040220](https://doi.org/10.3390/min9040220)
45. Jorgensen FRA, Moyle FJ. Phases formed during the thermal analysis of pyrite in air. *J Therm Anal.* 1982;25:473–485. doi:[10.1007/BF01912973](https://doi.org/10.1007/BF01912973)
46. Aracena Á, Jerez Ó, Colás Ortíz R, Morales JW. Pyrite oxidation kinetics in an oxygen-nitrogen atmosphere at temperatures from 400 to 500 °C. *Can Metall Q.* 2016;55:195–201. doi:[10.1080/00084433.2015.1126904](https://doi.org/10.1080/00084433.2015.1126904)
47. Reimers GW, Hjelmstad KE. Analysis of the oxidation of chalcocopyrite, chalcocite, galena, pyrrhotite, marcasite and arsenopyrite. Department of the Interior, Bureau of Mines. Report of investigations 9118 (United States. Bureau of Mines). Pittsburgh, Pa. U.S.: 1987.
48. Malek TJ, Chaki SH, Deshpande MP. Structural, morphological, optical, thermal and magnetic study of mackinawite FeS nanoparticles synthesized by wet chemical reduction technique. *Physica B: Condensed Matter.* 2018;546:59–66. doi:[10.1016/j.physb.2018.07.024](https://doi.org/10.1016/j.physb.2018.07.024)
49. Asaki Z, Matsutomo T, Tanabe T, Condo Y. Oxidation of Dense Iron Sulfide. *Metall Mater Trans. B.* 1983;14:109–116. doi:[10.1007/BF02670877](https://doi.org/10.1007/BF02670877)
50. Kennedy T, Sturman BT. The Oxidation of Iron (II) Sulfide. *J Therm Anal.* 1975;8:329–37. doi:[10.1007/BF01904010](https://doi.org/10.1007/BF01904010)
51. Asaki Z, Condo Y. Oxidation Kinetics of Iron Sulfide in the Form of Dense Plate, Pellet and Single Particle 1989;35:1751–1759. doi:[10.1007/BF01911664](https://doi.org/10.1007/BF01911664)

52. Coombs PG, Munir ZA. The mechanism of oxidation of ferrous sulfide (FeS) powders in the range of 648 to 923 K. *Metall Mater Trans B*. 1989;20:661–667. doi:[10.1007/BF02655922](https://doi.org/10.1007/BF02655922)
53. Gulyaeva RI, Selivanov EN, Vershinin AD. Nonisothermal Oxidation of Pyrrhotines. *Russian Metallurgy (Metally)*. 2003;4:299–304.
54. Alksnis A, Li B, Elliott R, Barati M. Kinetics of Oxidation of Pyrrhotite. In: B. Davis et al., editors. *Extraction 2018, The Minerals, Metals & Materials Series*. Cham: Springer; pp. 403–413. doi:[10.1007/978-3-319-95022-8_32](https://doi.org/10.1007/978-3-319-95022-8_32)
55. Habashi F, Dugdale R. The action of sulfur trioxide on chalcopyrite. *Metall Mater Trans. B*. 1973;4:1553–1556. doi:[10.1007/BF02668007](https://doi.org/10.1007/BF02668007)
56. Leung L.S. The overall kinetics of roasting of chalcopyrite. *Metall Mater Trans. B*. 1975;6:341–343. doi:[10.1007/BF02913578](https://doi.org/10.1007/BF02913578)
57. Aneesuddin M, Char PN, Hussain MR, Saxena ER. Studies on thermal oxidation of chalcopyrite from Chitradurga, Karnataka State, India. *J Therm Anal*. 1983;26:205–215. doi:[10.1007/BF01913204](https://doi.org/10.1007/BF01913204)
58. Chaubal PC, Sohn HY. Intrinsic kinetics of the oxidation of chalcopyrite particles under isothermal and nonisothermal conditions. *Metall Mater Trans. B*. 1986;17:51–60. doi:[10.1007/BF02670818](https://doi.org/10.1007/BF02670818)
59. Cocić MB, Logar MM, Cocić SLj, Dević SS, Manasijević DM. Transformation of chalcopyrite in the roasting process of copper concentrate in fluidized bed reactor. *JOM*. 2011;63:55–59. doi:[10.1007/s11837-011-0078-2](https://doi.org/10.1007/s11837-011-0078-2)
60. Živcović Ž, Štrbač N, Živcović D, Velinovski V, Mihajlović I. Kinetic study and mechanism of chalcocite and covellite oxidation process. *J Therm Anal Calorim*. 2005;79:715–720. doi:[10.1007/s10973-005-0601-1](https://doi.org/10.1007/s10973-005-0601-1)
61. Ramakrishna Rao VVVNS, Abraham KP. Kinetics of oxidation of copper sulfide. *Metall Mater Trans B*. 1971;2:2463–2470. doi:[10.1007/BF02814883](https://doi.org/10.1007/BF02814883)
62. Dunn JG, Ginting AR, O'Connor B. A thermoanalytical study of the oxidation of chalcocite. *J Therm Anal*. 1994;41:671–686. doi:[10.1007/BF02549341](https://doi.org/10.1007/BF02549341)
63. Benlyamani M, Ajersch F. Agglomeration of particles during roasting of zinc sulfide concentrates. *Metall Mater Trans B*. 1986;17:647–656. doi:[10.1007/BF02657127](https://doi.org/10.1007/BF02657127)
64. Dimitrov R, Bonev I. Mechanism of zinc sulphide oxidation. *Thermochim Acta*. 1986;106:9–25. doi:[10.1016/0040-6031\(86\)85111-5](https://doi.org/10.1016/0040-6031(86)85111-5)
65. Dimitrov RI, Boyanov BS. Oxidation of Metal Sulphides and Determination of Characteristic Temperatures by DTA and TG. *J Therm Anal Calorim*. 2000;61:181–189. doi:[10.1023/A:1010181112713](https://doi.org/10.1023/A:1010181112713)
66. Graydon JW, Kirk DW. A Microscopic study of the transformation of sphalerite particles during the roasting of zinc concentrate. *Metall Mater Trans. B*. 1988;19:141–146. doi:[10.1007/BF02666500](https://doi.org/10.1007/BF02666500)
67. Gulyaeva RI, Selivanov EN, Pikalov SM. Mechanism and Kinetics of the Thermal Oxidation of Natural Sphalerite. *Russian Metallurgy (Metally)*. 2018;3:221–227. doi:[10.1134/S0036029518030047](https://doi.org/10.1134/S0036029518030047)
68. Natesan K, Philbrook WO. Oxidation kinetic studies of zinc sulfide in a fluidized bed reactor. *Metall Mater Trans B*. 1970;1:1353–60. doi:[10.1007/BF02900254](https://doi.org/10.1007/BF02900254)
69. Marzoughi O, Halali M, Moradkhani D, Pickle CA. Kinetics of Roasting of a Sphalerite Concentrate. In: B. Davis et al., editors. *Extraction 2018, The Minerals, Metals & Materials Series*. Cham: Springer, 2018. doi:[10.1007/978-3-319-95022-8_44](https://doi.org/10.1007/978-3-319-95022-8_44)
70. Asaki Z, Nitta M, Tanabe T, Condo Y. Oxidation of cobalt sulfide. *Metall Mater Trans B*. 1986;17:367–373. doi:[10.1007/BF02655084](https://doi.org/10.1007/BF02655084)
71. Boyanov BS. Differential thermal study of the interactions between sulphates, oxides and ferrites. *Thermochim Acta*. 1997;302:109–115. doi:[10.1016/S0040-6031\(97\)00199-8](https://doi.org/10.1016/S0040-6031(97)00199-8)
72. Tsukada H, Asaki Z, Tanabe T, Condo Y. Oxidation of mixed copper-iron sulfide. *Metall Mater Trans B*. 1981;12:603–609. doi:[10.1007/BF02654333](https://doi.org/10.1007/BF02654333)
73. Arkhangel'sky IV, Dunaev AV, Makarenko IV, Tikhonov NA, Belyaev SS, Tarasov AV. Non-isothermal kinetic methods. *Workbook and Laboratory Manual*. Edition Open Access. 2013. <http://edition-open-access.de/media/textbooks/1/Textbooks1.pdf>. Accessed 23 Aug 2022.
74. Chung FH. A new X-ray diffraction method for quantitative multicomponent analysis. *Adv X-Ray Anal*. 1973;17:106–115. doi:[10.1154/S0376030800005231](https://doi.org/10.1154/S0376030800005231)
75. Hubbard CR, Evans EH, Smith DK. The reference intensity ratio, I/I_c , for computer simulated powder patterns. *J Appl Crystallogr*. 1976;9:169–174. doi:[10.1107/S0021889876010807](https://doi.org/10.1107/S0021889876010807)
76. Altomare A, Corriero N, Cuocci C, Falcicchio A, Moliterni A, Rizzi R. QUALX2.0: a qualitative phase analysis software using the freely available database POW_COD. *J Appl Crystallogr*. 2015;48:598–603. doi:[10.1107/S1600576715002319](https://doi.org/10.1107/S1600576715002319)
77. Arshad MA, Maaroufi AK. Recent advances in kinetics and mechanisms of condensed phase processes: a mini-review. *Rev Adv Mater Sci*. 2017;51:177–187.
78. Vyazovkin S, Burnham AK, Criado JM, Perez-Maqueda LA, Popescu C, Sbirrazzuoli N. ICTAC kinetics committee recommendations for performing kinetic computations on thermal analysis data. *Thermochim Acta*. 2011;520:1–19. doi:[10.1016/j.tca.2011.03.034](https://doi.org/10.1016/j.tca.2011.03.034)
79. Henderson DW. Thermal analysis of non-isothermal crystallization kinetics in glass forming liquids. *J Non-Cryst Solids*. 1979;30:301–315. doi:[10.1016/0022-3093\(79\)90169-8](https://doi.org/10.1016/0022-3093(79)90169-8)
80. Kissinger HE. Variation of peak temperature with heating rate in differential thermal analysis. *J Res Natl Bur Stand*. 1956;57:217–221.
81. Augis JA., Bennett JE. Calculation of the Avrami parameters for heterogeneous solid state reactions using a modification of the Kissinger method. *J Therm Anal*. 1978;13:283–292. doi:[10.1007/BF01912301](https://doi.org/10.1007/BF01912301)
82. Pelovski YG, Petkova V. Mechanism and kinetics of inorganic sulphates decomposition. *J Therm Anal*. 1997;49:1227–1241. doi:[10.1007/BF01983679](https://doi.org/10.1007/BF01983679)
83. Horoshavin AG. Forsterite 2MgO·SiO₂. Moscow: Teplotekhnik; 2004 (In Russian).
84. Yamaguchi T, Shiraishi T. Kinetic Studies of Eutectoid Decomposition of CuFe₂O₈. *J Am Ceram Soc*. 1971;54:556–558. doi:[10.1111/j.1151-2916.1971.tb12206.x](https://doi.org/10.1111/j.1151-2916.1971.tb12206.x)
85. Luo YH, Zhu DQ, Pan J, Zhou XL. Thermal decomposition behaviour and kinetics of Xinjiang siderite ore. *Mineral Processing and Extractive Metallurgy*. 2016;125:17–25. doi:[10.1080/03719553.2015.1118213](https://doi.org/10.1080/03719553.2015.1118213)
86. Petkova V, Pelovski YG. Comparative DSC study on thermal decomposition of iron sulphates. *J Therm Anal Calorim*. 2008;93:847–852. doi:[10.1007/S10973-008-9302-X](https://doi.org/10.1007/S10973-008-9302-X)
87. Petkova V, Pelovski YG, Paneva D, Mitov I. Influence of gas media on the thermal decomposition of second valence iron sulphates. *J Therm Anal Calorim*. 2011;105:793–803. doi:[10.1007/S10973-010-1242-6](https://doi.org/10.1007/S10973-010-1242-6)
88. Choi K, Kim S, Kim M, Park H. Oxidation Behavior of Copper Concentrate, Gold Concentrate, and Their Mixtures Between 1173 K (900 °C) and 1373 K (1100 °C). *Metall Mater Trans B*. 2019;50:1300–1308. doi:[10.1007/s11663-019-01575-3](https://doi.org/10.1007/s11663-019-01575-3)
89. Matusita K, Sakka S. Kinetic study of crystallization of glass by differential thermal analysis – criterion on application of Kissinger plot. *J Non-Cryst Solids*. 1980;38–39(2):741–746. doi:[10.1016/0022-3093\(80\)90525-6](https://doi.org/10.1016/0022-3093(80)90525-6)